

Electrochemical Properties of Three $\text{Li}_2\text{Ni}_2\text{TeO}_6$ Structural Polymorphs

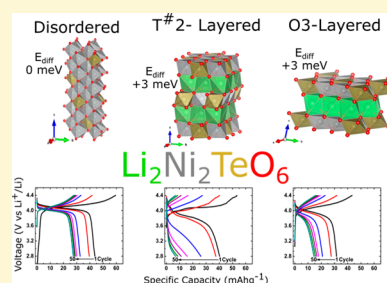
Nicholas S. Grundish,^{*,†,‡,§} Ieuan D. Seymour,^{‡,§} Graeme Henkelman,^{‡,§} and John B. Goodenough^{*,†,§}

[†]Materials Science and Engineering Program and Texas Materials Institute, The University of Texas at Austin, Austin, Texas 78712, United States

[‡]Department of Chemistry and the Oden Institute for Computational Engineering and Sciences, The University of Texas at Austin, Austin, Texas 78712, United States

Supporting Information

ABSTRACT: Three different structures of the composition $\text{Li}_2\text{Ni}_2\text{TeO}_6$ have been synthesized and their electrochemical properties characterized: a disordered orthorhombic phase with tellurium ordering and strong Li/Ni cation mixing, a T[#]2-layered phase, and an O3-layered phase; each have a distinct cycling performance. The disordered orthorhombic structure is the most stable at room temperature and has the highest capacity with the lowest overpotential. The T[#]2 phase is the least stable and undergoes a phase transformation once lithium is extracted. Density functional theory calculations reconcile the relative structural stabilities and physical properties of each phase with their electrochemical performances. Calculations also confirmed experimental observations regarding the synthesis of each structure and indicated the mechanism for capacity fade of each $\text{Li}_2\text{Ni}_2\text{TeO}_6$ cathode. Strong tellurium–oxygen covalent bonding increases the voltage of the $\text{Ni}^{2+/3+}$ redox couple in each of these materials over what is normally observed in layered oxides.



INTRODUCTION

There is a continuously growing demand for electric power storage for portable electronic devices. This growing demand brings with it the need to investigate new cathode materials for rechargeable batteries as the price of elements used in traditional commercial Li-ion batteries, such as cobalt in LiCoO_2 , continues to increase. Transition-metal elements such as nickel, manganese, and iron have been looked at as alternatives owing to their reduced cost and, in the case of nickel and manganese, the possibility of higher energy densities. There has been an exhaustive study of nickel-rich layered cathodes with the goal of maximizing the energy provided by the $\text{Ni}^{3+/4+}$ redox couple.^{1–5} Additionally, doping strategies have been investigated for minimizing Li/Ni cation mixing in these materials, which often severely deteriorates battery performance.^{6–9} Although these studies have provided some incremental advances in cathode alternatives, further materials exploration is necessary.

Disordered rock-salt materials have provided specific capacities beyond those of traditional layered lithium cathodes where they allow use of some redox energy of the oxygen anion as well as that of the transition metal cation.^{10–12} However, these materials are still in their infancy and usually need to be heated above room temperature to allow for any Li^+ diffusion at all. Heavier elements are usually avoided for use in electrode materials since they decrease the specific capacity as well as the overall gravimetric energy density of the cell, but their effects on lithium insertion/extraction and nickel diffusion remain relatively unstudied. Heavy ions in high oxidation states, such as Sb^{5+} and Te^{6+} , have shown promise in P2 and O3 layered

sodium cathode materials.^{13–16} This P2 and O3 nomenclature starts with a letter indicative of the site the alkali ion of the material occupies (P for prismatic, O for octahedral, or T for tetrahedral) and ends with the number of transition metal layers in the unit cell.^{15,16} The Sb and Te atoms form layered compounds with a honeycomb ordering of cations in the $\text{M}'_{2/3}\text{M}''_{1/3}\text{O}_2$ layer ($\text{M}' = \text{Co}/\text{Ni}$, $\text{M}'' = \text{Sb}/\text{Te}$). This honeycomb ordering lowers the energy pathway for sodium conduction in the sodium layers as it allows the sodium to avoid the Coulombic repulsion from the large-valence cations as it conducts through the adjacent sodium layers.^{17,18}

O3-layered $\text{Li}_3\text{Ni}_2\text{SbO}_6$ has been previously synthesized via an ion-exchange reaction from O3- $\text{Na}_3\text{Ni}_2\text{SbO}_6$ by using molten LiNO_3 , but it was shown to have significant capacity fade through the first 10 charge/discharge cycles owing to low-energy barriers for Ni transition from the transition metal MO_2 layer to the lithium layer.¹⁹ A composition containing tellurium of the form $\text{Li}_4\text{NiTeO}_6$ with an O3-layered stacking was shown to have decent electrochemical performance, delivering $\approx 100 \text{ mA h g}^{-1}$ over 100 charge/discharge cycles by removing reversibly 2 lithium atoms per formula unit on the $\text{Ni}^{2+/3+}$ and $\text{Ni}^{3+/4+}$ redox couples.²⁰ Another compound in the same material family is $\text{Li}_2\text{Ni}_2\text{TeO}_6$ (LNTO) with a reasonable theoretical specific capacity of $151.05 \text{ mA h g}^{-1}$; it has previously been prepared in a disordered orthorhombic phase and an unidentified layered

Received: July 24, 2019

Revised: October 7, 2019

Published: October 7, 2019

phase, but their electrochemical properties were never characterized.²¹

We have prepared three different structures of $\text{Li}_2\text{Ni}_2\text{TeO}_6$ and investigated their phase chemistry and electrochemical properties. The previously unidentified layered phase synthesized by an ion-exchange process with the sodium analogue in molten LiNO_3 was found to have a $T^{\#2}$ -layered structure. When this $T^{\#2}$ structure is heated, it forms a new O3-layered structure that has hitherto not been reported. The disordered orthorhombic rock-salt phase was the only phase that could be directly synthesized with lithium precursors by a solid-state method; it allows reversible insertion/extraction of the most lithium of any of the structures at room-temperature. However, each structure suffers from significant capacity fade upon cycling. This capacity fade in the disordered and O3-layered structures is attributed to Ni^{2+} transfer to the lithium layer as lithium is extracted from the material, preventing reinsertion of lithium upon discharge of the material. The $T^{\#2}$ structure suffered a much more profound capacity loss upon cycling than the other two structures owing to gliding of the transition metal layers upon lithium extraction of the material to form an O2-layered structure that is not electrochemically active in the range 2.8–4.4 V versus Li^+/Li .

EXPERIMENTAL AND COMPUTATIONAL METHODS

Disordered $\text{Li}_2\text{Ni}_2\text{TeO}_6$ was synthesized with a small amount of NiO impurity by mixing stoichiometric amounts of Li_2CO_3 (Acros Organics, 99+%), NiO (Alfa Aesar, 99%), and TeO_2 (Acros Organics, 99+%) in a mortar and pestle until a homogeneous mixture was obtained. Pellets of the precursor were pressed and fired at 900 °C for 24 h with a 10 °C/min heating and cooling rate. The $T^{\#2}$ -layered $\text{Li}_2\text{Ni}_2\text{TeO}_6$ was obtained through an ion-exchange procedure by using LiNO_3 with the corresponding P2-layered sodium compound $\text{Na}_2\text{Ni}_2\text{TeO}_6$ prepared as previously described.^{14,21} P2- $\text{Na}_2\text{Ni}_2\text{TeO}_6$ was prepared as a precursor for the ion exchange reaction by mixing stoichiometric amounts of Na_2CO_3 (Acros Organics, 99.8%), NiO, and TeO_2 in a mortar and pestle and heating to 650 °C for 12 h with a 10 °C/min heating/cooling rate. The resulting powder was reground, pressed into a pellet, and then fired at 810 °C for 24 h with a 2 °C/min heating rate and a 10 °C/min cooling rate. The resulting $\text{Na}_2\text{Ni}_2\text{TeO}_6$ powder was combined in a Pyrex beaker with 10 times its weight in LiNO_3 and heated to 300 °C for 4 h with a 10 °C/min heating rate. The beaker was allowed to cool down to room temperature in air before being sonicated with deionized water to dissolve residual LiNO_3 and NaNO_3 . The ion-exchanged $\text{Li}_2\text{Ni}_2\text{TeO}_6$ powder was recovered from the solution and washed via vacuum filtration. O3-layered $\text{Li}_2\text{Ni}_2\text{TeO}_6$ was obtained by heating the $T^{\#2}$ $\text{Li}_2\text{Ni}_2\text{TeO}_6$ powder to 800 °C for 6 h with a 10 °C/min heating and cooling rate.

X-ray diffraction (XRD) for structural analysis was performed on the resulting powders with a Rigaku Miniflex 600 (Cu $K\alpha$ radiation, $\lambda = 1.514$ Å) in Bragg–Brentano geometry. The 2θ range from 10° to 100° was scanned in step-scan mode with a step size of 0.02° and a dwell time of 2 s at each step. A structural model for the $T^{\#2}$ -LNTO structure was developed by first indexing the powder diffraction pattern with MDI Jade software and assigning atoms to different Wyckoff positions based on the stoichiometry of the compound. The structural model for the O3 compound was developed by comparison with the structurally analogous $\text{Na}_3\text{Ni}_2\text{SbO}_6$ compound. Rietveld structure refinement was performed on the resulting diffraction patterns with Fullprof, which verified the solved $T^{\#2}$ and O3 structures as well as the proper synthesis of the disordered orthorhombic phase that has previously been reported. The structural transition from $T^{\#2}$ to O3 stacking was mapped with an in situ heating X-ray diffraction set up in a Scintag X1 theta–theta diffractometer (Cu $K\alpha$ radiation, $\lambda = 1.514$ Å) at a scanning rate of 1°/min from $2\theta = 10^\circ$ to $2\theta = 60^\circ$. Powder XRD patterns were recorded from 25 to 800 °C in 100 °C increments starting at 100 °C.

The powder was heated at a rate of 10 °C/min and kept at each temperature for 1 h before a powder pattern was recorded to ensure any structural transformations had some time to develop.

Each material was ball-milled for 1 h in a hardened steel jar with a SPEX 8000 Mixer/Mill to reduce the particle size for electrochemical testing. Scanning electron microscopy (SEM) of the as prepared and ball-milled materials was conducted with a Hitachi S5500 SEM/STEM at an accelerating voltage of 20 kV. Electrode slurries were prepared by magnetic stir mixing ball-milled powder of each material (70 wt %) with Denka black (25 wt %) and 4 wt % polyvinylidene fluoride (PVDF) in *n*-methyl-2-pyrrolidone (NMP) such that the final weight of the PVDF in the electrode was 5 wt %. The electrode slurries were left to stir for 12 h prior to being blade coated onto a carbon-coated aluminum foil where the NMP was evaporated at 100 °C in a drying oven. After the NMP had been evaporated from the electrode slurries, leaving a uniform electrode coating on the foil, the electrodes were dried at 60 °C in vacuum for 12 h before coin cells were assembled. The 2032 coin cells were assembled in an MBraun glovebox under an inert argon atmosphere (O_2 : <0.1 ppm, H_2O : <0.1 ppm) with 1 M LiClO_4 EC:DMC (50:50) electrolyte and a lithium metal anode. All coin cells were galvanostatically cycled at a C/20 rate between 2.8 and 4.4 V on a Lanhe battery tester.

Electrodes for ex situ XRD were prepared with ball-milled active material powder (70 wt %), Denka black (25 wt %), and polytetrafluoroethylene (PTFE, 5 wt %). Each ball-milled LNTO powder was thoroughly mixed with Denka black before adding the PTFE and rolling into a thin composite electrode. These electrodes were dried at 80 °C prior to cell assembly. Ex situ XRD was performed on each polymorph of LNTO after a first charge to 4.4 V, after a first discharge to 2.8 V, and also after the 20th discharge down to 2.8 V to observe structural changes to each material upon repeated Li^+ insertion/extraction. Ex situ XRD was performed with a Rigaku Miniflex 600 as mentioned previously.

The energies of the disordered, $T^{\#2}$, O3, O2, and O6 structures of $\text{Li}_2\text{Ni}_2\text{TeO}_6$ were compared with first-principles calculations. All energies and forces in this work were calculated with DFT by using the projector augmented wave (PAW) approach in the VASP code.^{22,23} The Perdew–Burke–Ernzerhof (PBE) functional was used unless otherwise noted.²⁴ The *s* states were treated as valence for Li and the *p* states treated as valence for Ni, and the conventional pseudopotentials were used for O and Te in this study. The Ni 3d states required a Hubbard *U* correction (DFT+*U*) to correct for errors in the electron localization behavior inherent in conventional DFT.²⁵ The rotationally invariant version of DFT+*U* proposed by Dudarev et al. was used with a U_{eff} value of 6.2 eV for Ni, consistent with previous work.^{26,27} All calculations performed in this work were spin polarized.

Energetics of Li ordering in the disordered, $T^{\#2}$, and O3 $\text{Li}_2\text{Ni}_2\text{TeO}_6$ structures were studied by enumerating different configurations in the CASM package.^{28,29} Lattice parameters and atomic positions of the enumerated structures were optimized in the ferromagnetic state until the force on any atom was smaller than 0.05 eV/Å, with an energy convergence criterion of 1×10^{-6} eV. The Brillouin zone was sampled with a Γ -centered *k*-point mesh (mesh density ≥ 20 Å) and a plane-wave cut off of 520 eV. The lowest energy structures on the energy hull were optimized again with a tighter force tolerance of 0.01 eV/Å.

For the disordered *Fddd* structure, 810 Li–Ni orderings were enumerated in a small unit cell structure of $\text{Li}_2\text{Ni}_2\text{TeO}_6$ containing 22 atoms. The electrostatic energy of each structure was evaluated with an Ewald method in the GULP code.³⁰ The 60 lowest energy structures were then selected for further study with first-principles calculations. In the O3 $\text{Li}_x\text{Ni}_2\text{TeO}_6$ system, Li-vacancy orderings were investigated at Li compositions of $x = 0, 0.5, 1, 1.5, \text{ and } 2$. Starting from a *C2/m* structure with a honeycomb ordering of Ni and Te ions in the MO_2 layer, a total of 39 Li-vacancy orderings were enumerated over the octahedral sites in the Li layer.

There are three possible LiO_4 tetrahedral sites in the Li layer of the $T^{\#2}$ structure.^{31,32} The 8e sites are distorted LiO_4 tetrahedra that share edges with MO_6 octahedra in adjacent layers. As a result of the Ni–Te honeycomb ordering in the *Cmca* unit cell, the 8e sites can either share edges with two Ni ($8e_{\text{Ni:Ni}}$) or one Ni and one Te ($8e_{\text{Ni:Te}}$) site. The

other two positions in the Li layer are the $8f_{\text{edge}}$ and $8f_{\text{face}}$ sites, which share three edges with MO_6 octahedra and one face with a single MO_6 octahedron, respectively. A Monte Carlo (MC) based basin hopping technique was used with first-principles calculations to predict the lowest energy Li ordering of the $T^{\#2}$ -layered $\text{Li}_2\text{Ni}_2\text{TeO}_6$ end member. An 88 atom supercell of $T^{\#2}$ - $\text{Li}_2\text{Ni}_2\text{TeO}_6$ was created containing 16 Li atoms on $8e_{\text{Ni:Ni}}$ sites. A Li ion was selected and swapped with a vacant $8e$ or $8f_{\text{edge}}$ site at each Monte Carlo step, followed by full structural relaxation of the cell vectors and atomic positions. The 150 MC swaps were performed at a MC temperature of 600 K. Minimizing the computational cost required a softer pseudopotential set consisting of the conventional pseudopotentials for the cation species (Li, Ni, and Te) and a soft pseudopotential for O (O_{s}) with the Brillouin zone sampled at a single Γ point. Energy and force criteria of 1×10^{-5} eV and 0.1 eV/Å were used for each MC step, respectively, with a plane wave cut off energy of 400 eV. Starting from the lowest energy $T^{\#2}$ structure found from the MC simulations, a total of 31 Li orderings of the $8e$ and $8f_{\text{edge}}$ sites were calculated at compositions of $x = 0, 0.5, 1, \text{ and } 1.5$.

Structural transformations from $T^{\#2}$ to O2 or O6 phases can take place during electrochemical cycling.^{31,33} Therefore, a total of 41 and 39 Li-vacancy orderings were investigated for O2 and O6 $\text{Li}_x\text{Ni}_2\text{TeO}_6$ phases, respectively, at Li compositions of $x = 0, 0.5, 1, 1.5, \text{ and } 2$. A honeycomb ordering of Ni and Te within the MO_6 layer was also adopted for these structures with the same Ni–Te superstructure ordering along the c -axis as the $T^{\#2}$ structure. Previous studies have proposed three different Li sites within the Li layer in both the O2 and the O6 structures (Figure 1): (1) tetrahedral sites that share edges with

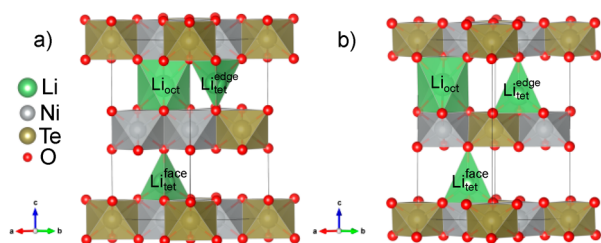


Figure 1. Schematic of the three types of Li sites in the (a) O2 and (b) O6 structures of $\text{Li}_x\text{Ni}_2\text{TeO}_6$: octahedral Li (Li_{oct}), tetrahedral sites sharing an edge with the Ni_2Te layer ($\text{Li}_{\text{tet}}^{\text{edge}}$), and tetrahedral sites sharing a face with the Ni_2Te layer ($\text{Li}_{\text{tet}}^{\text{face}}$).

three MO_6 octahedra, (2) tetrahedral sites that share a face with a MO_6 octahedron, and (3) octahedral sites that share a face with an MO_6 octahedron. In the O2- LiCoO_2 system, tetrahedral sites that share faces with an MO_6 site are high energy configurations.³² Thus, they were not considered in our enumeration. To limit the number of configurations for the O2 and O6 structures, we only considered configurations in which either the tetrahedral or octahedral sublattice was occupied in the enumeration. The $T^{\#2}$, O2, and O6 structures were also optimized with the opt86b-vdw functional and the same Hubbard U correction as used previously to study the effects of dispersion on the relative energies of the structures.^{34–36} For clarity, the two types of DFT+ U calculations with and without the dispersion correction will subsequently be referred to as opt86b-vdw+ U and PBE+ U , respectively.

Migration barriers for Ni diffusion in disordered, $T^{\#2}$, O2, and O3 structures upon delithiation were investigated with the climbing image nudged elastic band (CI-NEB) approach.³⁷ The 80-atom supercells of the lowest energy disordered, $T^{\#2}$, O2, and O3 LNTO structures from their respective convex hulls were optimized to a force tolerance of 0.01 eV/Å with the opt86b-vdw+ U functional. Possible Li/Ni migration mechanisms were then studied with CI-NEB under fixed volume conditions with the force on all images relaxed to a tolerance of 0.01 eV/Å.

RESULTS AND DISCUSSION

Crystal Structure and Synthesis. The energy hull for each structure is shown in Figures S1–3 (Supporting Information).

The lowest energy structures of the disordered, $T^{\#2}$, and O3 $\text{Li}_2\text{Ni}_2\text{TeO}_6$ phases are shown in Figure 2, with the corresponding calculated unit cell parameters shown in Table S1.

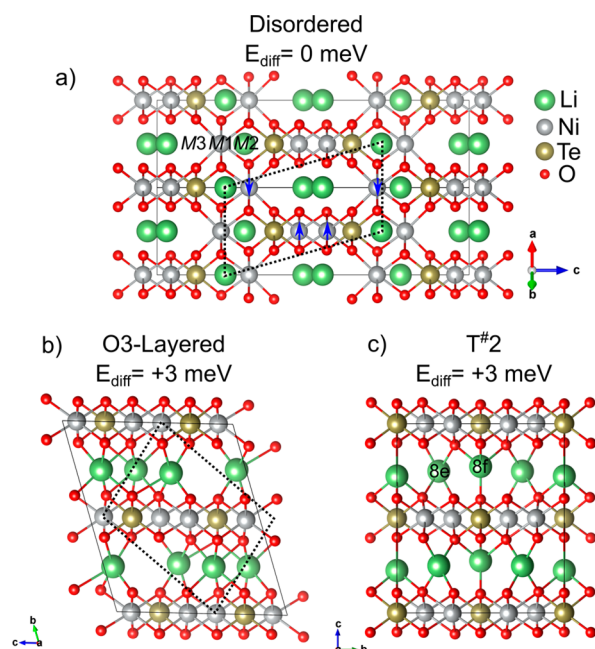


Figure 2. Lowest energy $\text{Li}_2\text{Ni}_2\text{TeO}_6$ structures of (a) disordered orthorhombic ($Fddd$) and (b) O3 (layered) and (c) $T^{\#2}$ $\text{Li}_2\text{Ni}_2\text{TeO}_6$ phases predicted by DFT. The difference in the energy per atom (E_{diff}) relative to the disordered structure is given. The dashed boxes indicate the unit cell structure used for calculations. The positions of the three metal sites (M1–M3) in the disordered $Fddd$ structure are noted. Spin alignment of the lowest energy antiferromagnetic ordering in the disordered structure is indicated with blue arrows. The $8e$ and $8f_{\text{Ni:Ni}}$ Li sites in the $T^{\#2}$ structure are indicated.

Figure 3 shows a Rietveld refinement and structural depiction of the orthorhombic disordered rock-salt LNTO. This structure has the $Fddd$ space group and is composed of face-sharing MO_6 octahedra with Te ordered on the $8a$ Wyckoff position. Lithium and nickel atoms share the occupancy of the $8b$ and $16g$ sites, providing a large amount of cation mixing. PBE+ U calculations showed that this orthorhombic disordered rock-salt structure

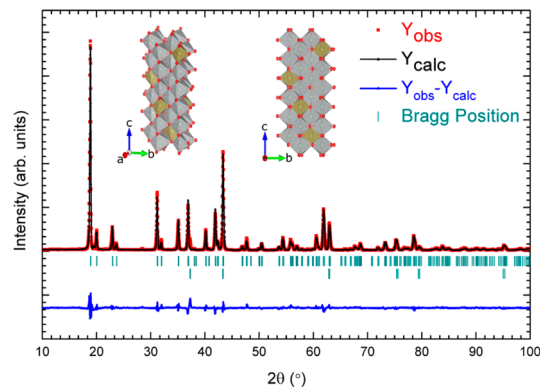


Figure 3. Rietveld refinement of the powder XRD pattern of disordered orthorhombic $\text{Li}_2\text{Ni}_2\text{TeO}_6$ ($R_{\text{Bragg}} = 6.0$ and $R_{\text{f}} = 5.99$); structure schematic inset with Li/Ni sites in silver octahedra, Te sites in gold octahedra, and O atoms as red spheres.

was lower in energy than the T[#]2 and O3 structures. This result is consistent with the observation that the disordered structure was the only phase that could be directly synthesized by solid-state reaction. The lowest energy disordered structure predicted from first-principles (Figure 2a) showed preferential occupancy of the M1 (Ni preference), M2 (Li preference), and M3 (vacancy preference) sites in the *Fddd* structure; it agrees with the experimentally observed site preferences. Antiferromagnetic ordering of the Ni²⁺ (*S* = 1) spins, as shown in Figure 2a, was 4 meV/atom lower in energy than the ferromagnetic ordering as a result of the 180° Ni–O–Ni configurations in the structure, which are expected to be strongly antiferromagnetic. Full occupation of the M1 and M2 sites with Ni²⁺ and Li⁺, respectively, results in tunnels along the $\langle 110 \rangle$ directions of the cell containing infinite Li chains that may act as channels for Li diffusion. However, partial occupation of Ni in the M2 and M3 sites may impede Li motion along these channels.

A T[#]2 layered structure was obtained by an ion-exchange reaction starting with the sodium analogue Na₂Ni₂TeO₆ with molten LiNO₃. A Rietveld refinement and structural model for the T[#]2 structure are depicted in Figure 4. This structure has

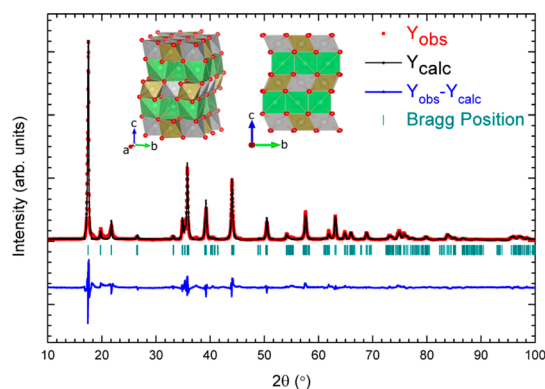


Figure 4. Rietveld refinement of powder XRD pattern of T[#]2 stacking Li₂Ni₂TeO₆ ($R_{\text{Bragg}} = 10.2$ and $R_f = 11.0$); structure schematic inset with Li sites as green tetrahedra, Ni sites as silver octahedra, Te sites as gold octahedra, and O atoms as red spheres.

alternating layers of lithium and MO₂ in the form of Ni_{2/3}Te_{1/3}O₂ where the Ni and Te display a honeycomb ordering indigenous to the layered antimonates and tellurates. The lowest energy structure predicted for the T[#]2 structure after 150 MC steps at 600 K consists of an ordered 1:1 arrangement of 8e_{Ni:Ni} and 8f_{edge} sites in an orthorhombic structure with *Pnma* space group. The 44-atom unit cell of this structure, as shown in Figure 2c, was fully optimized under tighter energy and force constraints. This unit cell was found to be 27 meV/atom lower in energy than the structure containing only 8e_{Ni:Ni} sites from PBE+U calculations. The presence of both 8e and 8f_{edge} sites is consistent with the previous studies on T[#]2 systems.³² The energy of the T[#]2 structure is 3 meV/atom higher than the disordered structure, highlighting the difficulty in direct synthesis of this phase. The energy of the T[#]2-layered phase is within DFT error of the O3-layered phase, which was an initial indication that the O3 phase could be obtained upon heating the T[#]2 phase if it could not be directly synthesized by a solid-state reaction.

Direct synthesis of an O3 structure by solid-state reaction at high temperature (1000–1200 °C) in an effort to obtain a phase transition from disordered to ordered resulted in the formation

of the known Li₄NiTeO₆ phase and excess NiO.²⁰ After failing to obtain directly the O3 structure, we explored the idea of heating the T[#]2 phase to high temperature. Figure 5 shows the results of an in situ heating X-ray diffraction experiment in which the transformation from T[#]2 to O3 stacking is observed. The significant decrease in layer spacing shown by the increase in the 2θ position of the primary (001) peak should be noted. This structural transition proposes that O3 is a more energetically favorable stacking structure since the T[#]2 structure is simply the result of a distortion from trigonal prismatic coordination in the alkali-ion layer in Na₂Ni₂TeO₆ to a tetrahedral coordination when the Na is exchanged for Li.

Figure 6 shows a Rietveld refinement and structural depiction of the O3-layered LNTO obtained after heating the T[#]2-layered LNTO at 800 °C for 6 h. As with the T[#]2 phase, the Ni and Te maintain a honeycombed ordering in the MO₂ layers, but the lithium atoms now occupy octahedral sites within the lithium layer. The calculated lowest energy O3 structure (Figure 2b) was found to be 3 meV/atom higher in energy than the disordered Li₂Ni₂TeO₆ structure. The similarity in the energy of the T[#]2 and O3 phases is consistent with the high temperature (~600 °C) of the T[#]2 → O3 transformation. The relative stability of the T[#]2 phase in Li₂Ni₂TeO₆ is in contrast to the O2 phase of LiCoO₂, which undergoes an O2 → O3 phase transformation at ~290 °C.³⁸ Previous ab initio calculations of the O2-LiCoO₂ system suggest that the O2 structure is 14 meV/atom higher in energy than the O3-LiCoO₂ structure, leading to a lower transformation temperature.³² A summary of the crystallographic data for each synthesized structure of Li₂Ni₂TeO₆ can be found in Table S2 (Supporting Information).

Electrochemical Characterization. SEM images showing the morphology of each material as-prepared and after ball milling are shown in Figure S4 (Supporting Information). The large size of the as-prepared particles was a concern when assessing how much lithium could be extracted from each structure; therefore, ball-milling for particle-size reduction was a precaution in order to gain an accurate representation of the lithium insertion/extraction capabilities of each phase. Galvanostatic charge/discharge performance of all three structures of LNTO are portrayed in Figure 7. Although a small amount of capacity fade after the first few cycles is expected owing to the formation of a solid electrolyte interphase (SEI), the T[#]2 structure showed a far more significant capacity fade than the disordered and O3 structures. The O3 phase showed poor Coulombic efficiency throughout cycling compared to the disordered phase. T[#]2 layered LNTO showed Coulombic efficiencies of over 100% on some cycles indicating irreversible structural transformations were occurring.

Each structure exhibited lithium intercalation/deintercalation around the same voltage range (3.9–4.1 V) operating on the Ni^{2+/3+} redox couple as shown by the galvanostatic cycling curves given in Figure 8. This voltage is slightly higher than what is normally expected for the Ni-based redox in layered structures,^{6,7} but it can be attributed to an increase in the covalency owing to strong Te–O bonding. This high degree of covalent bonding results in an inductive effect that increases the voltage of the Ni^{2+/3+} redox couple.²⁰

Of the three structures, the disordered structure allowed for the most lithium to be reversibly inserted/extracted from the structure with the lowest overpotential. Partial occupation by Ni in the M2 and M3 sites may block lithium diffusion in the $\langle 110 \rangle$ tunnels of the orthorhombic structure, but the ability to extract

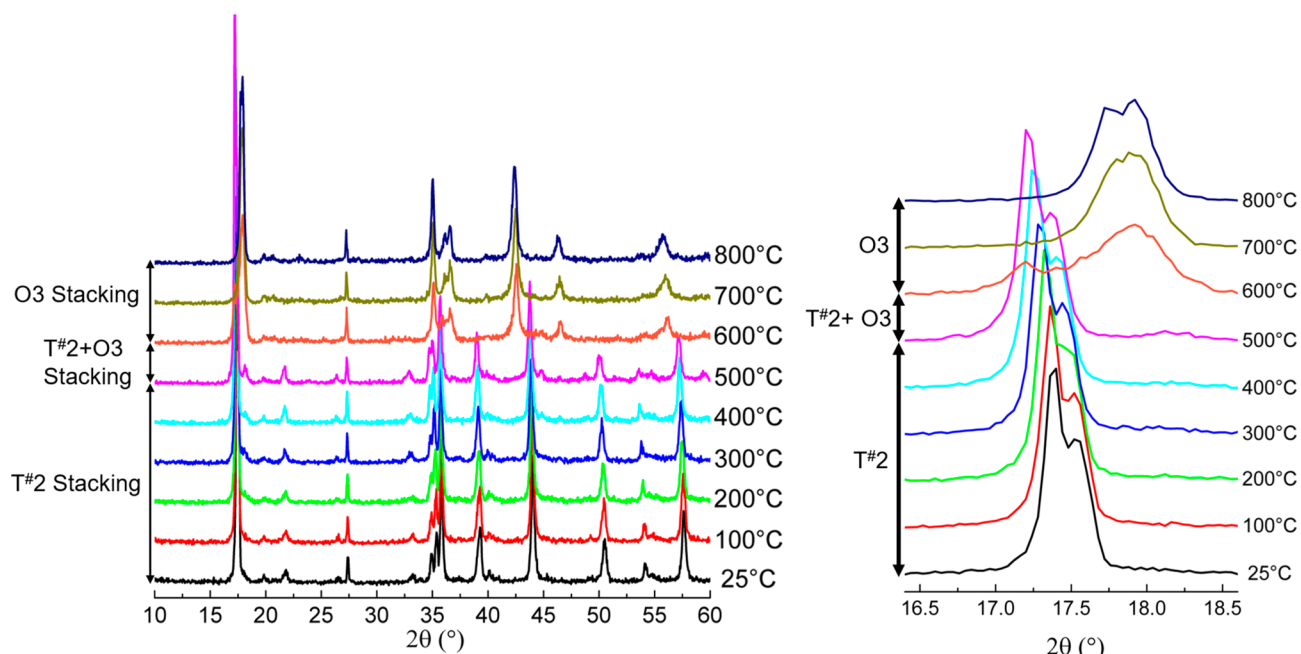


Figure 5. Powder XRD patterns obtained in situ during heating of the T^{#2} Li₂Ni₂TeO₆ from 25 to 800 °C; enlarged view of the first Bragg reflection of each pattern.

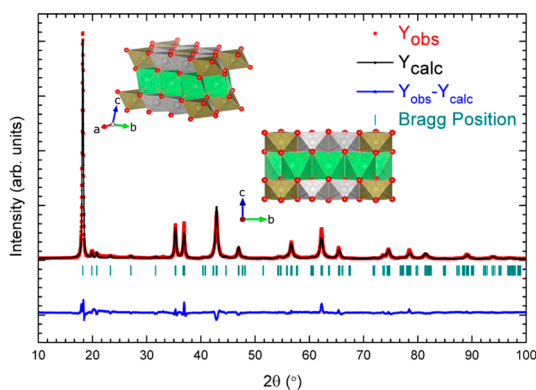


Figure 6. Rietveld refinement of the room-temperature powder XRD pattern of O3 stacking Li₂Ni₂TeO₆ ($R_{\text{Bragg}} = 9.92$ and $R_f = 7.71$); structure schematic inset with Li sites as green octahedra, Ni sites as silver octahedra, Te sites as gold octahedra, and O atoms as red spheres.

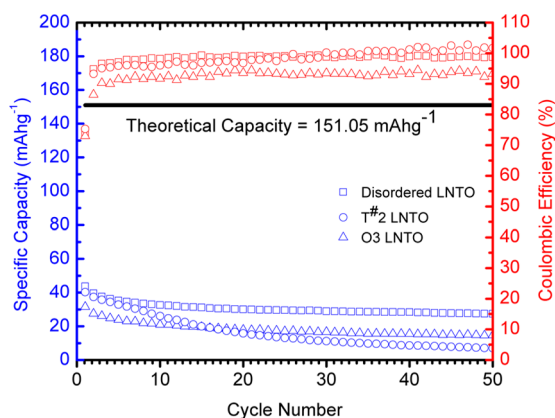


Figure 7. Specific capacity and Coulombic efficiency of the three structural polymorphs of Li₂Ni₂TeO₆ for 50 charge/discharge cycles.

Li from the structure reversibly indicates that some of the Li can migrate. Thus, Li/Ni mixing in this structure does not allow for an unimpeded pathway for lithium diffusion as in either of the layered structures. The energy of the Li_xNi₂TeO₆ structure on delithiation was investigated computationally at $x = 0$ and 1 (Figure S1a, Supporting Information). At $x = 1$, the voltage to remove half the Li from each Li channel was predicted to be 4.28 V, which agrees with the experimentally observed voltage of 4.1 V. The removal of a second Li from the structure ($x = 0$) is predicted to occur at 4.65 V, which is above the upper cut off voltage of 4.4 V used in this study and may overlap with electrolyte oxidation.

Disordered rock-salt structures have been largely investigated for anion redox energies.^{13–15} However, in this material, delithiation results in the removal of electrons from Ni 3d states, although a significant density of O 2p states lay near the Fermi level at all states of charge as verified by the electronic density of states (DOS) plot developed from DFT (Figure S1b, Supporting Information). Additionally, DOS plots of the fully lithiated T^{#2} and O3 structures reveal a significant density of O 2p states near the Fermi level of these polymorphs as well (Figure S1c, Supporting Information). Ex situ X-ray diffraction of the disordered structure did not show any significant structural distortion upon lithium insertion/extraction from the material (Figure S5, Supporting Information). This lack of structural transformation led us to investigate whether nickel diffusion is a cause for capacity fade in this material as is discussed in depth below.

The energies of the T^{#2}, O2, and O6 structures on delithiation were also computationally studied as shown in Figure 9 and Figure S2 (Supporting Information). PBE+U predictions of the lowest energy O2 structure for the end member composition Li₂Ni₂TeO₆ contained Li in edge sharing tetrahedral sites, whereas the lowest energy O6 structure contained Li in octahedral sites. The O2 and O6 structures were, respectively, +6 and +13 meV/atom higher in energy than the T^{#2} structure.

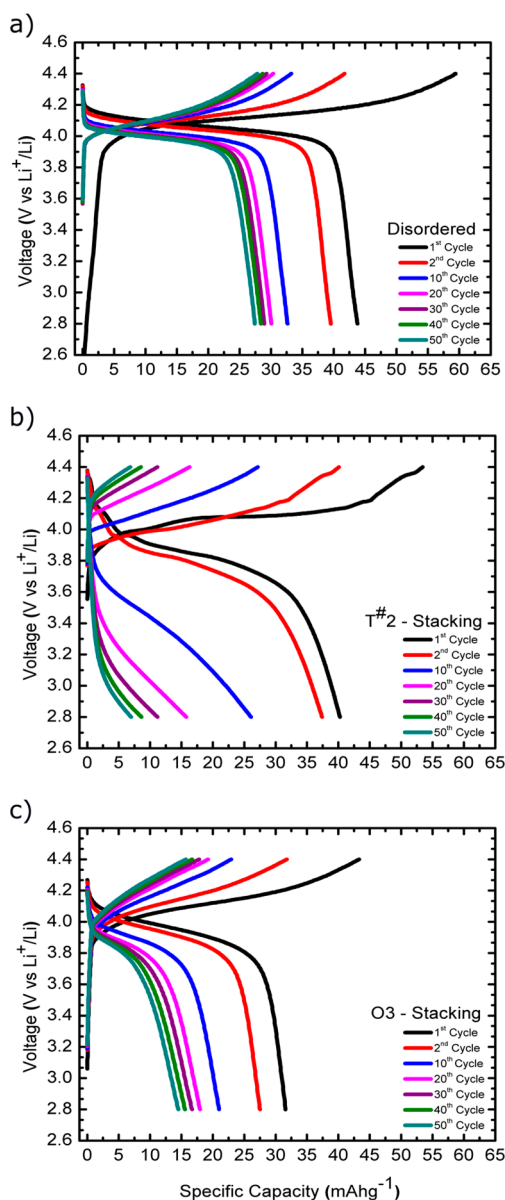


Figure 8. Galvanostatic charge/discharge profiles for (a) disordered orthorhombic, (b) T[#]2-stacked, and (c) O3-stacked Li_xNi₂TeO₆ cycled at a C/20 rate.

Different Li orderings of the 8e_{Ni:Ni} and 8f sites were enumerated for the T[#]2 phase, and stable Li orderings were found on the hull at LiNi₂TeO₆ and Li_{0.5}Ni₂TeO₆ from PBE+U. Li occupied the 8e_{Ni:Ni} sites, keeping the 8f sites vacant in both structures. For LiNi₂TeO₆, the energy of the structure containing only 8f sites was found to be +21 meV/atom higher in energy than the structure with only 8e_{Ni:Ni} sites. PBE+U predicted stable phases at LiNi₂TeO₆ ($x = 1$) for the O2 and O6 structures in which Li occupy edge sharing tetrahedral sites (Figure S2). The lowest energy O6 structure at $x = 1$ was +5 meV/atom higher in energy than the T[#]2 structure (Figure 9). The lowest energy O2 structure was 2 meV/atom lower in energy than the T[#]2 structure which indicates that there is a driving force to transform to the O2 phase. On full delithiation to Ni₂TeO₆ ($x = 0$), the O6 structure is predicted to be the lowest energy of the three phases by approximately 7 meV/atom. The structural transformation of the T[#]2 phase upon delithiation was experimentally investigated with ex situ X-ray

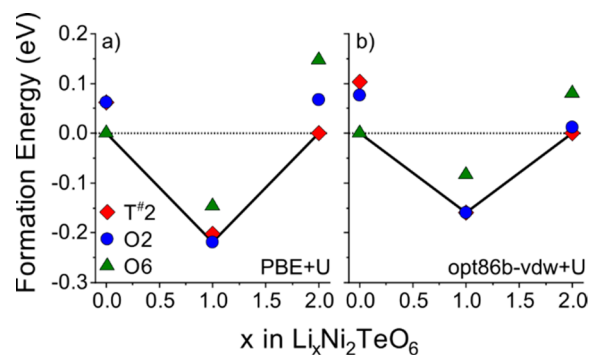


Figure 9. Convex energy hull (black line) of T[#]2, O2, and O6 Li_xNi₂TeO₆ structures calculated with (a) PBE+U and (b) opt86b-vdw+U functionals. The formation energy $E(\text{form})$ of the Li_xNi₂TeO₆ structures ($E_{\text{Li}x}$) is calculated relative to the lowest energy end member compositions of T[#]2 Li₂Ni₂TeO₆ ($E_{\text{O}2-\text{Li}2}$) and O6 Ni₂TeO₆ ($E_{\text{O}6-\text{Li}0}$) via the relation $E_{\text{form}} = E_{\text{Li}x} - (x/2)E_{\text{O}2-\text{Li}2} - (1 - x/2)E_{\text{O}6-\text{Li}0}$.

diffraction (Figure 10 and Figure S6, Supporting Information). Upon first charge to 4.4 V, the T[#]2-layered phase transformed

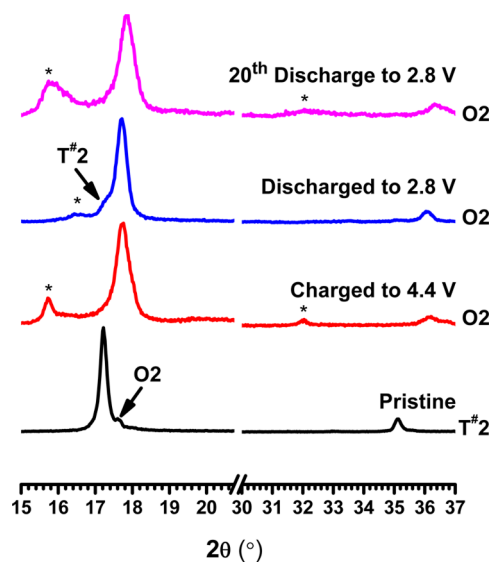


Figure 10. Ex situ powder XRD of T[#]2-stacked Li_xNi₂TeO₆ electrodes showing the phase transformation to O2-stacking and another unknown phase designated by *.

into an O2-layered phase and a second phase that could not be identified, designated by the formation of peaks at 15.6° and 32° 2θ in the diffraction pattern. This phenomenon has been previously seen in the O2-LiCoO₂ system.³³ The structural transformation is quasi-reversible upon first discharge as the 2θ attributed to the unknown phase decreases in intensity in comparison to the O2 (001) peak and a small amount of T[#]2-layered phase is reformed. However, upon further insertion/extraction of lithium into the material, the structural transformation becomes less and less reversible until the intensity of the unknown phase peak becomes about half of the intensity of the O2 (001) peak on the 20th discharge. This change is reflected in the galvanostatic cycling curves as a vast reduction in the reversible specific capacity of the material in the first 10 cycles, which only becomes exponentially worse thereafter until negligible specific capacity of the material is seen after 50 charge/discharge cycles.

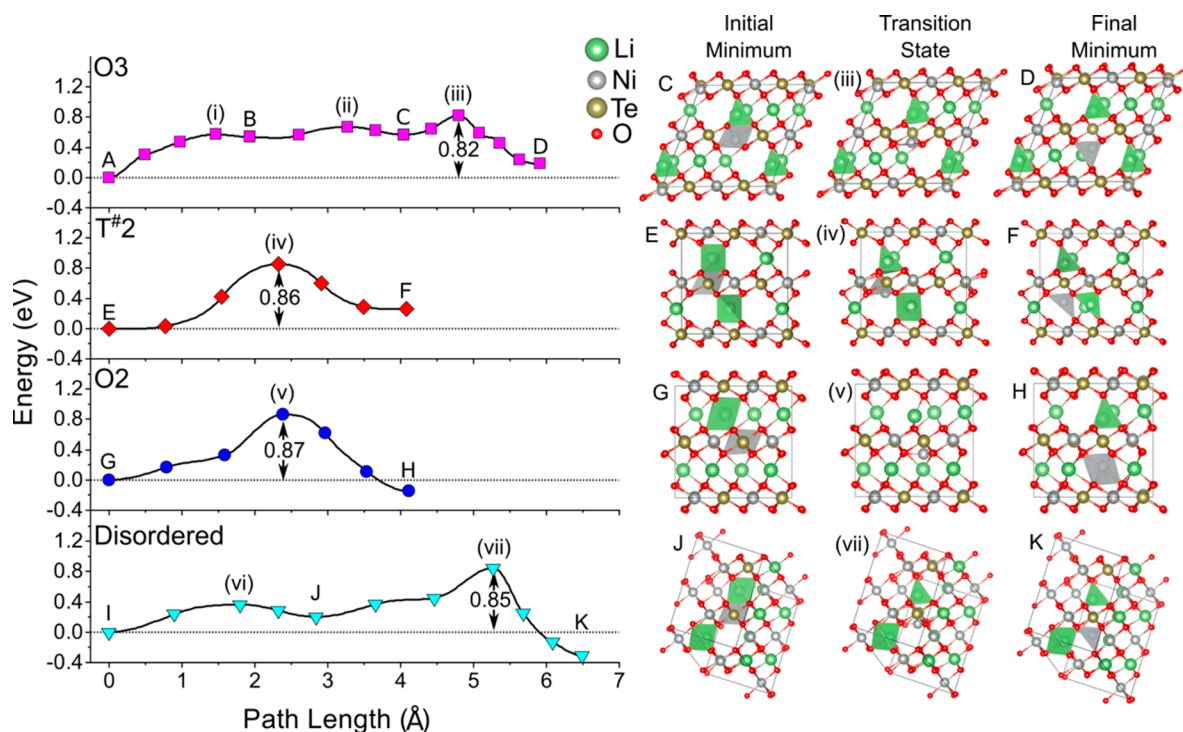


Figure 11. DFT migration barriers for Ni and Li in O3, T[#]2, O2, and disordered LiNi₂TeO₆ structures calculated with the opt86b-vdw+U functional. Minima are labeled A–K and transition states i–vii. The overall migration barrier in eV for Li/Ni diffusion in each structure is indicated with a black arrow. The structure of the local minima and transition states of the processes involving Ni diffusion are shown with the mobile atoms highlighted as polyhedral.

The difference among the T[#]2, O2, and O6 structures results from subtle stacking sequence changes between the Ni_{2/3}Te_{1/3} layers. Thus, the effect of including a dispersion correction in the DFT+U formalism was investigated with the opt86b-vdw functional (opt86b-vdw+U). The same Li-ordering at $x = 1$ for the T[#]2 structure was obtained with opt86b-vdw+U where the 8e_{Ni,Ni} sites were fully occupied. Upon relaxation, several of the delithiated T[#]2 structures relaxed to O2 structures via a shifting of the Ni_{2/3}Te_{1/3} layers. The lowest energy O2 and O6 structures at Li₂Ni₂TeO₆ ($x = 2$) and LiNi₂TeO₆ ($x = 1$) contained Li on octahedral sites (Figure S2). At $x = 1$, the energies of the lowest O2 and T[#]2 structures were within DFT error of each other for opt86b-vdw+U (Figure 9b), whereas the energy of the O6 structure was +7 meV/atom higher. The fully delithiated O6 structure was again lower in energy than the O2 and T[#]2 phases. The structural changes during delithiation from T[#]2 → O2 → O6 predicted with the opt86b-vdw+U functional is consistent with the results in the absence of a dispersion correction (PBE+U). However, the inclusion of a dispersion correction appears to stabilize the octahedral coordination of Li in the O2 and O6 structures.

Stable Li orderings of the O3-layered structure on delithiation were predicted to be on the energy hull at $x = 0.5, 1,$ and 1.5 , as shown in Figure S3 (Supporting Information). Multiple metastable Li-orderings were within 10 meV/atom of the lowest energy structure for each configuration, suggesting that significant Li disorder will be present at room temperature as a result of thermal energy (~ 25 meV at 300 K). The voltages for the removal of 0.5, 1, 1.5, and 2 Li from the structure were predicted to be 4.15, 4.20, 4.57, and 4.69 V, respectively. As was the case for the disordered structure, the removal of >1 Li in the O3-Li₂Ni₂TeO₆ structure is expected to be above the voltage

window of the current study as well as to begin to overlap with the oxidation window of most organic liquid electrolytes.

The Ni^{2+/3+} redox plateau remains for the O3 structure through insertion/extraction of lithium. However, there is a decrease in specific capacity on subsequent cycles that is greater over the first 10 cycles than the subsequent 40 thereafter. With no structural changes evident from ex situ X-ray diffraction (Figure S7, Supporting Information), as in the disordered orthorhombic structure, we again turned to nickel transfer as a probable cause for this capacity fade as even at full charge to 4.4 V on first charge there is still about 1.5 Ni²⁺ per formula unit that can transfer to the Li galleries, limiting the amount of lithium that can insert back into the material.

Nickel Transfer. Structural changes owing to diffusion of transition metal ions between layers in layered LiMO₂ structures are a key factor that leads to capacity loss during cycling.^{39–41} Therefore, we chose to study the migration barriers of Ni ions in supercells of the lowest energy disordered, T[#]2, O2, and O3 Li_xNi₂TeO₆ ($x = 1$) structures. All migration barriers shown in Figure 11 were calculated with opt86b-vdw+U owing to the effect that dispersion corrections have been shown to have on Li site preference. First-principles calculations have shown that the initial migration of transition-metal ions in an O3 structure occurs from octahedral sites in the transition-metal layer to tetrahedral sites in the Li layer.³⁹ In the first stage of the process (A-i-B) (Figure 11 and Figure S8, Supporting Information), Li in the Li layer migrates from its initial position which forms a trivacancy into which Ni can diffuse. In configuration B, the Li ion occupies a tetrahedral coordination that is face sharing with a Ni²⁺ ion. This configuration is a shallow local minimum that is consistent with previous work on Li_xMnO₂.⁴² In the second stage of the process (B-ii-C), a second Li ion in an adjacent layer migrates to another tetrahedral site which is face sharing with a

Ni^{2+} ion. In the third stage of the process (C-iii-D), the Ni^{2+} ion migrates from the octahedral site to a tetrahedral site through the triangular face of the initial NiO_6 octahedron (Figure 11). The overall barrier for this migration process (A–D) is 0.82 eV. The magnetic moment of the diffusing Ni during the migration process are $1.73 \mu_B$ (C), $1.78 \mu_B$ (iii), and $-1.78 \mu_B$ (D), which is consistent with a constant oxidation state of Ni^{2+} . The negative magnetic moment in configuration D suggests that there is a preference for antiferromagnetic alignment between the tetrahedral Ni^{2+} site and the octahedral $\text{Ni}^{2+/3+}$ sites in the Ni layer.

A single migration process was found for the $T^{\#2}$ structure in which a Ni^{2+} ion diffuses from an octahedral site (E) to a distorted tetrahedral site (F) in the Li layer. Analogous to the O3 structure, the migration of Ni^{2+} in the $T^{\#2}$ structure also involves the migration of two Li ions, but with a cooperative mechanism without a shallow local minimum. As Ni^{2+} diffuses in the structure, a Li (8e) ion in the Li layer below is displaced to an adjacent Li (8f_{face}) site. Another Li(8e) ion then migrates to a tetrahedral site (Li_{tet}) above the newly created Ni vacancy (V_{Ni}) forming a Li_{tet}– V_{Ni} –Ni_{tet} dumbbell defect, similar to that present in the O3 structure.³⁹ The single Ni–Li correlated migration process had a migration barrier of 0.86 eV. Analysis of the magnetic moment on the diffusing Ni ion in E ($1.72 \mu_B$), iv ($1.78 \mu_B$), and F ($1.78 \mu_B$) indicates that the oxidation state remains Ni^{2+} as in the O3 structure.

The O2 structure consists of NiO_6 octahedra that share faces with a tetrahedral site in one Li layer and an octahedral site in the opposing Li layer. Several representative configurations were tested, and it was found that the energy of a Ni^{2+} in the octahedral site of the Li layer was lower in energy than the tetrahedral site by around 0.3 eV. Therefore, the Ni^{2+} octahedral site configuration was considered for analysis of the migration barrier. In the lowest energy ordering of the O2– $\text{LiNi}_2\text{TeO}_6$ structure, the octahedral site in the Li layer below a Ni^{2+} octahedral site is vacant. A possible migration process (Figure 11) involves direct diffusion of Ni from the octahedral site in the $\text{Ni}_{2/3}\text{Te}_{1/3}$ layer (G) to the vacant octahedral site in the Li layer (H) through a shared triangular octahedral face. During Ni migration, a Li_{oct} ion from an adjacent site migrates cooperatively to a tetrahedral site above the newly formed V_{Ni} site, forming a Li_{tet}– V_{Ni} –Ni_{oct} defect. The total barrier for the cooperative Li–Ni migration is 0.87 eV, and the oxidation state of Ni remains Ni^{2+} throughout the process.

A similar migration mechanism was observed in the disordered structure as in the O3 structure. The process begins (I–vi–J) with Li migration from an octahedral site to an adjacent octahedral site in the same tunnel via a tetrahedral site (Figure S8, Supporting Information). This diffusion of Li creates space for a Ni^{2+} ion in an octahedral site (J) on the edge of a $\langle 110 \rangle$ tunnel to diffuse into a tetrahedral site (K) in the tunnel leaving a nickel vacancy (V_{Ni}) behind. From the tetrahedral site, the Ni^{2+} finally transfers to an adjacent octahedral site within the same tunnel. The migrating Ni^{2+} ion is accompanied by a cooperatively migrating Li ion from an octahedral site to a tetrahedral site, which coordinates with the vacant V_{Ni} site. The overall barrier for migration is 0.85 eV and the magnetic moments of the diffusing Ni ion are $1.74 \mu_B$ (J), $1.78 \mu_B$ (vii), and $-1.78 \mu_B$ (K), indicating a constant oxidation state of Ni^{2+} as with the previous structures. Comparison of the disordered and the O3-layered structure shows that the presence of tetrahedral Li sites that share faces with Ni octahedra (structures B and C) in the O3-layered structure are more stable as opposed to a

tetrahedral Li coordination that is formed when a V_{Ni} site is created as in the disordered structure (K).

The results in Figure 11 show that, regardless of the structure, migration barriers for Ni^{2+} diffusion are fairly constant from 0.82 to 0.87 eV. The Ni^{2+} migration barriers in these compounds are in line with the barriers previously found with DFT+U for Ni migration in $\text{LiNi}_{2/3}\text{Sb}_{1/3}\text{O}_2$ (0.63 eV), which was also shown to degrade structurally during cycling.¹⁹ The oxidation state of Ni plays a crucial role on the size of the migration barrier. Nickel with higher oxidation states ($\text{Ni}^{3+/4+}$) is expected to have larger barriers due to an increase in the octahedral site preference that prevents migration through tetrahedral sites to get to octahedral sites in adjacent lithium layers.¹⁹ The incorporation of Te^{6+} only increases the fraction of Ni^{2+} in the material throughout the insertion/extraction of lithium in these $\text{Li}_2\text{Ni}_2\text{TeO}_6$ compounds, leading to rapid phase transformations and Ni^{2+} diffusion in these materials.

CONCLUSION

Three structural polymorphs of the stoichiometry $\text{Li}_2\text{Ni}_2\text{TeO}_6$ have been synthesized and their electrochemical performance evaluated. All three structures exhibited a higher voltage than expected for the $\text{Ni}^{2+/3+}$ redox couple of around 3.9–4.1 V owing to strong Te–O covalent bonding. None of the structures synthesized approached the theoretical capacity of the $\text{Li}_2\text{Ni}_2\text{TeO}_6$ composition of 151 mA h g^{-1} , but the disordered orthorhombic structure showed the best electrochemical performance.

The disordered structure was the easiest to synthesize owing to its low energy of formation relative to other possible atomic arrangements such as a $T^{\#2}$, O2, or O3 layered structures of $\text{Li}_2\text{Ni}_2\text{TeO}_6$. Lithium and nickel cation mixing hinders the conduction of lithium along $\langle 110 \rangle$ pathways in the disordered structure that would appear if lithium and nickel did not mix, but the ability to extract lithium in an electrochemical cell demonstrates that the tunnels are not completely blocked when the material is prepared.

$T^{\#2}$ -layered $\text{Li}_2\text{Ni}_2\text{TeO}_6$ was synthesized by an ion exchange reaction with P2-layered $\text{Na}_2\text{Ni}_2\text{TeO}_6$. However, computations and ex situ X-ray diffraction of the material showed a quick and severe phase transformation from $T^{\#2}$ to O2 stacking upon lithium extraction from the structure is favorable and indeed occurs. The transformation seems quasi-reversible at first but is incomplete until lithium can no longer be inserted/extracted from the material in a meaningful capacity. The O2 phase does not seem electrochemically active in the 2.8–4.4 V voltage range of this study. The capacity fade of the $T^{\#2}$ material upon transformation to the O2 phase is greater than even the capacity fade of the O3-layered material which undergoes severe nickel transfer from the transition metal layer into the lithium layer. Other than Ni^{2+} transfer, the O3-layered phase does not undergo any further structural transformation upon cycling.

The nickel transfer in the $T^{\#2}$ and O3 layered structures was relegated to transfer of Ni^{2+} to an adjacent lithium layer via a tetrahedral or octahedral site. For the disordered structure the transferred nickel rests in the $\langle 110 \rangle$ tunnels. The barriers for nickel diffusion in each structure were low and similar to each other even with varying mechanisms. This result suggests that Ni^{2+} transfer may plague any layered structure that it inhabits despite its octahedral-site preference energy. The unidentified phase formed as well as the O2 layered phase upon delithiation of the $T^{\#2}$ structure may be the result of a surface reconstruction

that inhibits lithium insertion/extraction into the O2-layered phase.

■ ASSOCIATED CONTENT

Supporting Information

The Supporting Information is available free of charge on the ACS Publications website at DOI: [10.1021/acs.chemmater.9b02956](https://doi.org/10.1021/acs.chemmater.9b02956).

Crystallographic information for the disordered rock-salt structure (CIF)

Crystallographic information for the O3 structure (CIF)

Crystallographic information for the T^{#2} structure (CIF)

Summary of crystallographic data for each synthesized structure; energy hull and DOS plot of the disordered structure; DOS plots for the T^{#2} and O3 structures; energy hulls of the T^{#2}, O2, O6, and O3 structures; ex situ XRD of the disordered, T^{#2}, and O3 structures; SEM of each material before and after ball-milling; and Li migration mechanism for the O3 and disordered structures (PDF)

■ AUTHOR INFORMATION

Corresponding Authors

*(N.S.G.) E-mail: nicholas.grundish@utexas.edu.

*(J.B.G.) E-mail: jgoodenough@mail.utexas.edu.

ORCID

Nicholas S. Grundish: 0000-0003-1821-6734

Graeme Henkelman: 0000-0002-0336-7153

John B. Goodenough: 0000-0001-9350-3034

Author Contributions

[#]N.S.G. and I.D.S. contributed equally to this work.

Notes

The authors declare no competing financial interest.

■ ACKNOWLEDGMENTS

G.H. and J.B.G. would like to acknowledge the support of the Robert A. Welch Foundation, Houston, Texas (Grant Nos. F-1066 and F-1841). N.S.G. would like to acknowledge financial support by the U.S. Department of Energy, Office of Basic Energy Sciences, Division of Materials Sciences and Engineering, under Award No. DE-SC0005397. Computational resources were provided by the Texas Advanced Computing Center and the National Energy Research Scientific Computing Center. The authors would like to acknowledge the X-ray diffraction facilities within the Texas Materials Institute.

■ REFERENCES

- (1) Ohzuku, T.; Makimura, Y. Layered Lithium Insertion Material of $\text{LiCo}_{1/3}\text{Ni}_{1/3}\text{Mn}_{1/3}\text{O}_2$ for Lithium-Ion Batteries. *Chem. Lett.* **2001**, *30* (7), 642–643.
- (2) Ohzuku, T.; Makimura, Y. Layered Lithium Insertion Material of $\text{LiNi}_{1/2}\text{Mn}_{1/2}\text{O}_2$: A Possible Alternative to LiCoO_2 for Advanced Lithium-Ion Batteries. *Chem. Lett.* **2001**, *30* (8), 744–745.
- (3) Koyama, Y.; Yabuuchi, N.; Tanaka, I.; Adachi, H.; Ohzuku, T. Solid-State Chemistry and Electrochemistry of $\text{LiCo}_{1/3}\text{Ni}_{1/3}\text{Mn}_{1/3}\text{O}_2$ for Advanced Lithium-Ion Batteries I. First-Principles Calculation on the Crystal and Electronic Structures. *J. Electrochem. Soc.* **2004**, *151* (10), A1545–A1551.
- (4) Koyama, Y.; Makimura, Y.; Tanaka, I.; Adachi, H.; Ohzuku, T. Systematic Research on Insertion Materials Based on Superlattice Models in a Phase Triangle of LiCoO_2 - LiNiO_2 - LiMnO_2 I. First-Principles Calculation on Electronic and Crystal Structures, Phase

Stability and New $\text{LiNi}_{1/2}\text{Mn}_{1/2}\text{O}_2$ Material. *J. Electrochem. Soc.* **2004**, *151* (9), A1499–A1506.

(5) Myung, S.-T.; Maglia, F.; Park, K.-J.; Yoon, C. S.; Lamp, P.; Kim, S.-J.; Sun, Y.-K. Nickel-Rich Layered Cathode Materials for Automotive Lithium-Ion Batteries: Achievements and Perspectives. *ACS Energy Letters* **2017**, *2* (1), 196–223.

(6) Ohzuku, T.; Ueda, A.; Nagayama, M. Electrochemistry and Structural Chemistry of LiNiO_2 (R3m) for 4 V Secondary Lithium Cells. *J. Electrochem. Soc.* **1993**, *140* (7), 1862–1870.

(7) Dahn, J. R.; von Sacken, U.; Jutzkow, M. W.; Al-Janaby, H. Rechargeable LiNiO_2 /Carbon Cells. *J. Electrochem. Soc.* **1991**, *138* (8), 2207–2211.

(8) Dahn, J. R.; von Sacken, U.; Michal, C. A. Structure and Electrochemistry of $\text{Li}_{1-x}\text{NiO}_2$ and a New Li_2NiO_2 Phase with the $\text{Ni}(\text{OH})_2$ Structure. *Solid State Ionics* **1990**, *44* (1), 87–97.

(9) Thomas, M. G. S. R.; David, W. I. F.; Goodenough, J. B.; Groves, P. Synthesis and Structural Characterization of the Normal Spinel $\text{Li}[\text{Ni}_2]\text{O}_4$. *Mater. Res. Bull.* **1985**, *20* (10), 1137–1146.

(10) Yabuuchi, N.; Takeuchi, M.; Nakayama, M.; Shiiba, H.; Ogawa, M.; Nakayama, K.; Ohta, T.; Endo, D.; Ozaki, T.; Inamasu, T.; et al. High-Capacity Electrode Materials for Rechargeable Lithium Batteries: Li_3NbO_4 -Based System with Cation-Disordered Rocksalt Structure. *Proc. Natl. Acad. Sci. U. S. A.* **2015**, *112* (25), 7650–7655.

(11) Lee, J.; Urban, A.; Li, X.; Su, D.; Hautier, G.; Ceder, G. Unlocking the Potential of Cation-Disordered Oxides for Rechargeable Lithium Batteries. *Science* **2014**, *343* (6170), 519–522.

(12) Urban, A.; Lee, J.; Ceder, G. The Configurational Space of Rocksalt-Type Oxides for High-Capacity Lithium Battery Electrodes. *Adv. Energy Mater.* **2014**, *4* (13), 1400478.

(13) Yuan, D.; Liang, X.; Wu, L.; Cao, Y.; Ai, X.; Feng, J.; Yang, H. A Honeycomb-Layered $\text{Na}_3\text{Ni}_2\text{SbO}_6$: A High-Rate and Cycle-Stable Cathode for Sodium-Ion Batteries. *Adv. Mater.* **2014**, *26* (36), 6301–6306.

(14) Gupta, A.; Buddie Mullins, C.; Goodenough, J. B. $\text{Na}_2\text{Ni}_2\text{TeO}_6$: Evaluation as a Cathode for Sodium Battery. *J. Power Sources* **2013**, *243*, 817–821.

(15) Delmas, C.; Fouassier, C.; Hagenmuller, P. Structural Classification and Properties of the Layered Oxides. *Physica B+C* **1980**, *99* (1), 81–85.

(16) Delmas, C.; Braconnier, J.-J.; Fouassier, C.; Hagenmuller, P. Electrochemical Intercalation of Sodium in Na_xCoO_2 Bronzes. *Solid State Ionics* **1981**, *3–4*, 165–169.

(17) Evstigneeva, M. A.; Nalbandyan, V. B.; Petrenko, A. A.; Medvedev, B. S.; Kataev, A. A. A New Family of Fast Sodium Ion Conductors: $\text{Na}_2\text{M}_2\text{TeO}_6$ (M = Ni, Co, Zn, Mg). *Chem. Mater.* **2011**, *23* (5), 1174–1181.

(18) Kumar, V.; Bhardwaj, N.; Tomar, N.; Thakral, V.; Uma, S. Novel Lithium-Containing Honeycomb Structures. *Inorg. Chem.* **2012**, *51* (20), 10471–10473.

(19) Ma, X.; Kang, K.; Ceder, G.; Meng, Y. S. Synthesis and Electrochemical Properties of Layered $\text{LiNi}_{2/3}\text{Sb}_{1/3}\text{O}_2$. *J. Power Sources* **2007**, *173* (1), 550–555.

(20) Sathiyaa, M.; Ramesha, K.; Rousse, G.; Foix, D.; Gonbeau, D.; Guruprakash, K.; Prakash, A. S.; Doublet, M. L.; Tarascon, J.-M. $\text{Li}_4\text{NiTeO}_6$ as a Positive Electrode for Li-Ion Batteries. *Chem. Commun.* **2013**, *49* (97), 11376.

(21) Kumar, V.; Gupta, A.; Uma, S. Formation of Honeycomb Ordered Monoclinic $\text{Li}_2\text{M}_2\text{TeO}_6$ (M = Cu, Ni) and Disordered Orthorhombic $\text{Li}_2\text{Ni}_2\text{TeO}_6$ Oxides. *Dalton Transactions* **2013**, *42* (42), 14992.

(22) Blöchl, P. E. Projector Augmented-Wave Method. *Phys. Rev. B: Condens. Matter Mater. Phys.* **1994**, *50* (24), 17953–17979.

(23) Kresse, G.; Furthmüller, J. Efficient Iterative Schemes for Ab Initio Total-Energy Calculations Using a Plane-Wave Basis Set. *Phys. Rev. B: Condens. Matter Mater. Phys.* **1996**, *54* (16), 11169–11186.

(24) Perdew, J. P.; Burke, K.; Ernzerhof, M. Generalized Gradient Approximation Made Simple. *Phys. Rev. Lett.* **1996**, *77* (18), 3865–3868.

(25) Anisimov, V. I.; Zaanen, J.; Andersen, O. K. Band Theory and Mott Insulators: Hubbard U Instead of Stoner I. *Phys. Rev. B: Condens. Matter Mater. Phys.* **1991**, *44* (3), 943–954.

(26) Dudarev, S. L.; Botton, G. A.; Savrasov, S. Y.; Humphreys, C. J.; Sutton, A. P. Electron-Energy-Loss Spectra and the Structural Stability of Nickel Oxide: An LSDA+U Study. *Phys. Rev. B: Condens. Matter Mater. Phys.* **1998**, *57* (3), 1505–1509.

(27) Wang, L.; Maxisch, T.; Ceder, G. Oxidation Energies of Transition Metal Oxides within the GGA+U Framework. *Phys. Rev. B: Condens. Matter Mater. Phys.* **2006**, *73* (19), 195107.

(28) Van der Ven, A.; Thomas, J. C.; Xu, Q.; Bhattacharya, J. Linking the Electronic Structure of Solids to Their Thermodynamic and Kinetic Properties. *Mathematics and Computers in Simulation* **2010**, *80* (7), 1393–1410.

(29) Van der Ven, A.; Thomas, J. C.; Xu, Q.; Swoboda, B.; Morgan, D. Nondilute Diffusion from First Principles: Li Diffusion in Li_xTiS_2 . *Phys. Rev. B: Condens. Matter Mater. Phys.* **2008**, *78* (10), 104306.

(30) Gale, J. D. GULP: A Computer Program for the Symmetry-Adapted Simulation of Solids. *J. Chem. Soc., Faraday Trans.* **1997**, *93* (4), 629–637.

(31) Tournadre, F.; Croguennec, L.; Saadoune, I.; Morcrette, M.; Willmann, P.; Delmas, C. The $\text{T}\#2\text{-Li}_{2/3}\text{Co}_{2/3}\text{Mn}_{1/3}\text{O}_2$ System. 2. Its Electrochemical Behavior. *Chem. Mater.* **2004**, *16* (8), 1418–1426.

(32) Carlier, D.; Van der Ven, A.; Delmas, C.; Ceder, G. First-Principles Investigation of Phase Stability in the $\text{O}_2\text{-LiCoO}_2$ System. *Chem. Mater.* **2003**, *15* (13), 2651–2660.

(33) Carlier, D.; Saadoune, I.; Ménétrier, M.; Delmas, C. Lithium Electrochemical Deintercalation from $\text{O}_2\text{-LiCoO}_2$ Structure and Physical Properties. *J. Electrochem. Soc.* **2002**, *149* (10), A1310–A1320.

(34) Klimeš, J.; Bowler, D. R.; Michaelides, A. Chemical Accuracy for the van Der Waals Density Functional. *J. Phys.: Condens. Matter* **2010**, *22* (2), 022201.

(35) Klimeš, J.; Bowler, D. R.; Michaelides, A. Van Der Waals Density Functionals Applied to Solids. *Phys. Rev. B: Condens. Matter Mater. Phys.* **2011**, *83* (19), 195131.

(36) Dion, M.; Rydberg, H.; Schröder, E.; Langreth, D. C.; Lundqvist, B. I. Van Der Waals Density Functional for General Geometries. *Phys. Rev. Lett.* **2004**, *92* (24), 246401.

(37) Henkelman, G.; Uberuaga, B. P.; Jónsson, H. A Climbing Image Nudged Elastic Band Method for Finding Saddle Points and Minimum Energy Paths. *J. Chem. Phys.* **2000**, *113* (22), 9901–9904.

(38) Paulsen, J. M.; Mueller-Neuhaus, J. R.; Dahn, J. R. Layered LiCoO_2 with a Different Oxygen Stacking (O_2 Structure) as a Cathode Material for Rechargeable Lithium Batteries. *J. Electrochem. Soc.* **2000**, *147*, 508–516.

(39) Reed, J.; Ceder, G.; Van Der Ven, A. Layered-to-Spinel Phase Transition in Li_xMnO_2 . *Electrochem. Solid-State Lett.* **2001**, *4* (6), A78–A81.

(40) Shao-Horn, Y.; Hackney, S. A.; Armstrong, A. R.; Bruce, P. G.; Gitzendanner, R.; Johnson, C. S.; Thackeray, M. M. Structural Characterization of Layered LiMnO_2 Electrodes by Electron Diffraction and Lattice Imaging. *J. Electrochem. Soc.* **1999**, *146* (7), 2404–2412.

(41) Peres, J. P.; Delmas, C.; Rougier, A.; Broussely, M.; Pertion, F.; Biensan, P.; Willmann, P. The Relationship between the Composition of Lithium Nickel Oxide and the Loss of Reversibility during the First Cycle. *J. Phys. Chem. Solids* **1996**, *57* (6), 1057–1060.

(42) Seymour, I. D.; Chakraborty, S.; Middlemiss, D. S.; Wales, D. J.; Grey, C. P. Mapping Structural Changes in Electrode Materials: Application of the Hybrid Eigenvector-Following Density Functional Theory (DFT) Method to Layered $\text{Li}_{0.5}\text{MnO}_2$. *Chem. Mater.* **2015**, *27* (16), 5550–5561.